Active Use of DFIG-Based Variable-Speed Wind-Turbine for Voltage Control in Power System Operation

Hee-Sang Ko†, Gi-Gab Yoon *, and Won-Pyo Hong**

Abstract – This paper presents an active use of doubly-fed induction-generator (DFIG)-based variable-speed wind-turbine for voltage control in power system operation. For reasonable simulation studies, a detail dynamic model of a DFIG-based wind-turbine grid-connected system is presented. For the research objective, an innovative reactive power control scheme is proposed that manipulates dynamically the reactive power from the voltage source converter (VSC) with taking into account its operating state and limits.

Keywords: Doubly Fed Induction Generator, Variable Speed Wind Turbine, Voltage Control, Voltage Source Converter

1. Introduction

Increased wind power generation has influenced the overall power system operation and planning in terms of power quality, security, stability, and voltage control [1] – [6]. The local power flow pattern and the system's dynamic characteristics change when large wind turbines (WTs) are connected to the utility grid [7].

Both fixed-speed and variable-speed WTs are presently used in Europe and North America. To achieve the required voltage regulation, fixed-speed WTs are often complemented by additional equipment and/or compensating devices that may be installed in close proximity or at a remote location [8] – [11]. Doubly fed induction generators (DFIGs) are also becoming popular for variable-speed WTs, particularly in North America, with the modern units often exceeding the 3MW level [12].

In many WT applications, variable-speed operation is achieved by appropriately controlling the back-to-back voltage source converters (VSC). There have been a great number of publications proposing various control solutions to achieve desirable dynamic performance and decoupled control of active and reactive power. Although different in implementation, most commonly used converters enable the WTs to maintain the required power factor (power factor control, PFC) or voltage (local voltage control, LVC) at the terminals [13] – [16]. The rotor-side converter provides the active and the reactive power necessary to attain the control objectives for either the PFC or the LVC modes. The grid-side converter is connected through the filter. Its main objective is to maintain the dc-link capacitor voltage by exchanging the active power with the grid. Consequently, PFC-mode is often used for maximum active power exchange with the grid.

Mostly, undesirably interfere with the protection circuitry and/or the trip of WTs are caused when dc-voltage in dc-link reaches its limit. From this point of view, it is desirable to minimize and/or suppress the voltage swings at the terminal of WT. To achieve this objective, an innovative reactive power control methodology is presented in the rotor-side converter and the grid-side converter.

This paper is organized as follows: The detail dynamic model is described in Section 2; in Section 3, the VSC control design is presented; the reactive power control design is proposed in Section 4; case studies are carried out in Section 5; and conclusions are drawn in Section 6.

2. Dynamic Model of DFIG-Based Variable-Speed Wind -Turbine

The system considered in this paper is shown in Fig. 1. WT is equipped with a step-up 0.69/34.5kV transformer (TR). The WT is connected to the grid using 1km cable. The WT is assumed to supply about 40% of active power to the local load installed at the point-of-common coupling (PCC, bus 3). The remaining active power is assumed to come through the 34.5kV transmission line (TL, 30km) from the utility grid, which is represented by an infinite bus. Also, from the WT, 60% reactive power is

† Corresponding Author: Korea Institute of Energy Reearch, Daejeon, Korea, (hee-sang@ieee.org).
* Korea Electric Power Research Institute, Daejeon, Korea, 305-380, (ykk@kepri.re.kr).
** Dept. of Building Services Engineering at the Hanbat National University, Daejeon, Korea, 305-719, (wphong@hanbat.ac.kr).
Received 24 April, 2007; Accepted: 15 February, 2008

assumed to supply to the local load and 40% reactive power is assumed to be sent to the grid. The details of the WT considered in the model are shown in Fig. 2. In this paper, the 2MW WT is considered [17]. The WT consists of the following components: a three-bladed rotor with the corresponding pitch controller; a mechanical gearbox; and a DFIG with two converters, dc-link capacitor, and a grid filter.

The electrical part of the overall system is modeled using the *dq*–synchronous reference frame representation of the individual components. Wherein, *d*-axis is assumed to be aligned to stator flux, and the current coming out of the machine is considered positive. The DFIG controllers utilize the concept of disconnection of the real and reactive power controls by transformation of the machine parameters into the *dq*-reference frame and by separating forming of the rotor voltages. Then, the real power can be controlled by influencing the *d*-axis component of the rotor current while the reactive power can be controlled by influencing the *q*-axis components of the rotor current. The mechanical dynamic models include the drive-train model and the pitch control and the system parameters, operating conditions, controller gains, etc., can be found in [18].

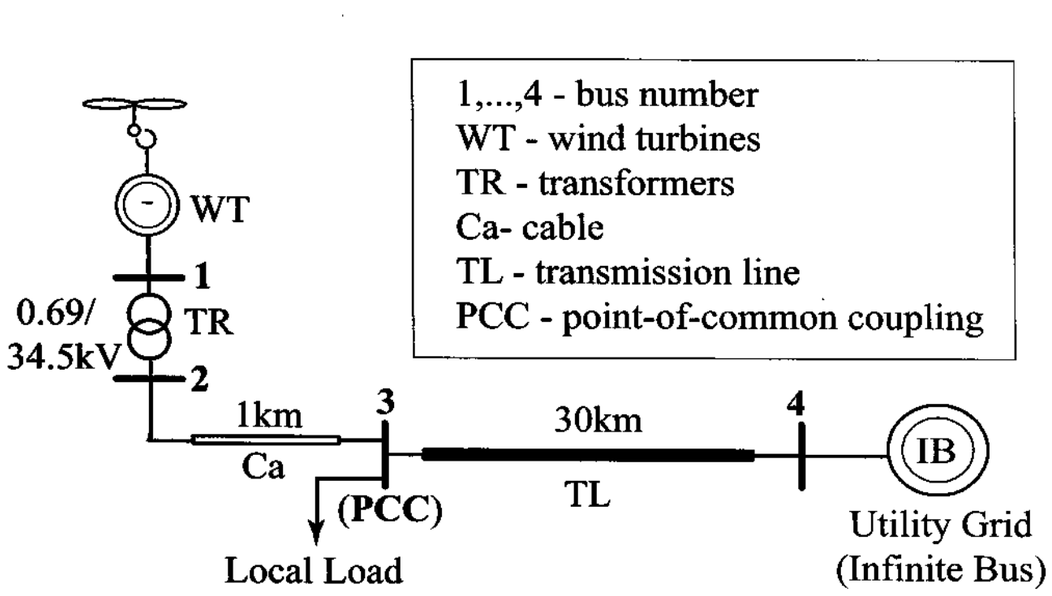

Fig. 1. Grid-connected wind turbine system.

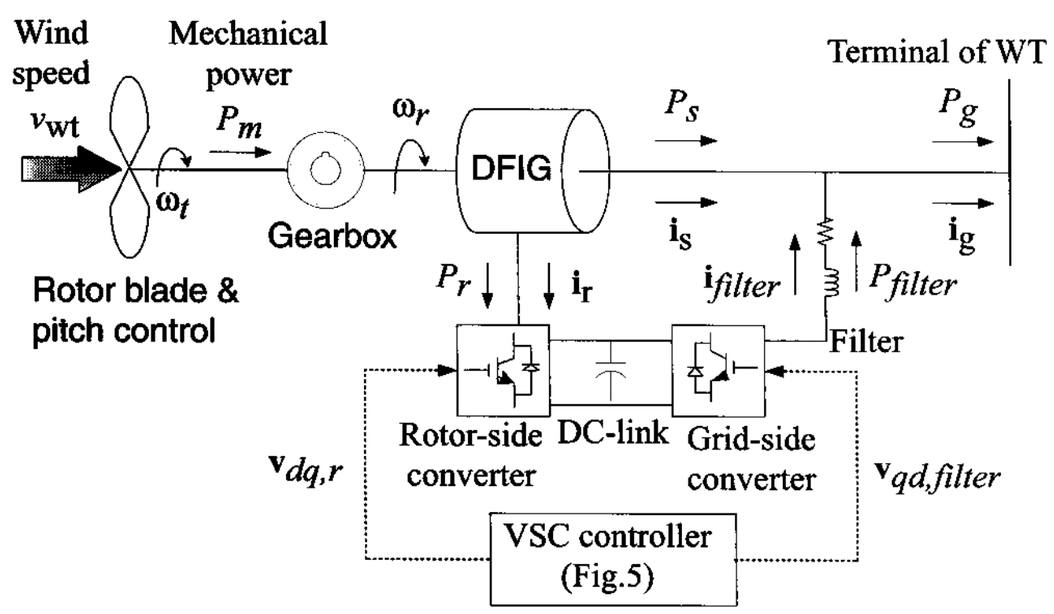

Fig. 2. Doubly fed induction generator wind turbine.

2.1 Doubly-Fed Induction Generator

The DFIG was represented by the following equations

$$\begin{aligned}
\frac{1}{\omega_b}\frac{d\psi_{ds}}{dt} &= R_s i_{ds} + \omega_e \psi_{qs} + v_{ds} \\
\frac{1}{\omega_b}\frac{d\psi_{qs}}{dt} &= v_{qs} + R_s i_{qs} - \omega_e \psi_{ds} \\
\frac{1}{\omega_b}\frac{d\psi_{dr}}{dt} &= v_{dr} + R_r i_{dr} + \omega_e \psi_{qr} \\
\frac{1}{\omega_b}\frac{d\psi_{qr}}{dt} &= v_{qr} + R_r i_{qr} - \omega_e \psi_{dr}
\end{aligned} \tag{1}$$

with

$$\begin{aligned}
\psi_{ds} &= -(L_s + L_m) i_{ds} - L_m i_{dr}, \quad \psi_{qs} = -(L_s + L_m) i_{qs} - L_m i_{qr} \\
\psi_{dr} &= -(L_r + L_m) i_{dr} - L_m i_{ds}, \quad \psi_{qr} = -(L_r + L_m) i_{qr} - L_m i_{qs}
\end{aligned} \tag{2}$$

where v is the voltage, R is the resistance, i is the current, ω_e and $\omega_s = \omega_e - \omega_r$ are the stator and slip electrical angular speed, respectively, ω_r is the rotor electrical angular speed, ω_b is the base angular speed in rad/sec, L_m is the mutual inductance, L_s and L_r are the stator and rotor leakage inductance, respectively, and ψ is the flux linkage. The subscripts *d* and *q* indicate the direct and quadrature axis components, respectively. The subscripts *s* and *r* indicate stator and rotor quantities, respectively. The electrical active and reactive power delivered by the stator are given by

$$P_s = v_{ds} i_{ds} + v_{qs} i_{qs}, \quad Q_s = v_{ds} i_{qs} - v_{qs} i_{ds} \tag{3}$$

2.2 Dynamic Mode of Transmission Line, Transformer, Cable and Load

The mathematical model of a TL, a TR, a cable, and a load can be found from the description of the R, L, C segment into the *dq*–synchronous reference frame [19]. The equations of the TL, the TR, the cable, and the RL-filter on the grid-side converter are given in (4) – (7), respectively. For the formulation of the TR and the load, for the numerical purpose, small capacitors $(C_o = 1e^{-6}$ p.u.) are used to the sending-end with removing two

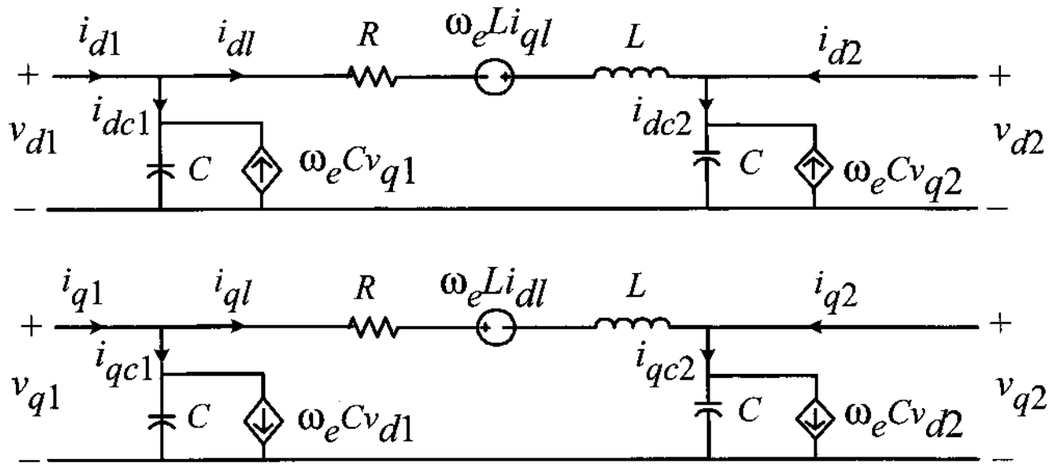

Fig. 3. Lumped TL description in the *dq*-domain.

capacitors, and the sending-end capacitors are only considered in the case of formulating the cable since its capacitance contributes to the reactive power.

Transmission line (TL)

$$\frac{L_{TL}}{\omega_b}\frac{di_{dl}}{dt} = v_{d1} - v_{d2} - R_{TL}i_{dl} + \omega_e L_{TL} i_{ql}$$

$$\frac{L_{TL}}{\omega_b}\frac{di_{ql}}{dt} = v_{q1} - v_{q2} - R_{TL}i_{ql} - \omega_e L_{TL} i_{dl}$$

$$\frac{C_{TL}}{\omega_b}\frac{dv_{d1}}{dt} = i_{dc1} + \omega_e C_{TL} v_{q1}, \quad \frac{C_{TL}}{\omega_b}\frac{dv_{q1}}{dt} = i_{qc1} - \omega_e C_{TL} v_{d1}$$

$$\frac{C_{TL}}{\omega_b}\frac{dv_{d2}}{dt} = i_{dc2} + \omega_e C_{TL} v_{q2}, \quad \frac{C_{TL}}{\omega_b}\frac{dv_{q2}}{dt} = i_{qc2} - \omega_e C_{TL} v_{d2} \tag{4}$$

where subscript 1 and 2 corresponds to bus 3 and bus 4, respectively.

Transformer (TR)

$$\frac{L_{tr}}{\omega_b}\frac{di_{dl}}{dt} = v_{d1} - v_{d2} - R_{tr}i_{dl} + \omega_e L_{tr} i_{ql}$$

$$\frac{L_{tr}}{\omega_b}\frac{di_{ql}}{dt} = v_{q1} - v_{q2} - R_{tr}i_{ql} - \omega_e L_{tr} i_{dl}$$

$$\frac{C_o}{\omega_b}\frac{dv_{d1}}{dt} = i_{dl} + \omega_e C_o v_{q1}, \quad \frac{C_o}{\omega_b}\frac{dv_{q1}}{dt} = i_{ql} - \omega_e C_o v_{d1} \tag{5}$$

where subscript 1 and 2 corresponds to bus 1 and bus 2, respectively.

Cable

$$\frac{L_{ca}}{\omega_b}\frac{di_{dl}}{dt} = v_{d1} - v_{d2} - R_{ca}i_{dl} + \omega_e L_{ca} i_{ql}$$

$$\frac{L_{ca}}{\omega_b}\frac{di_{ql}}{dt} = v_{q1} - v_{q2} - R_{ca}i_{ql} - \omega_e L_{ca} i_{dl}$$

$$\frac{C_{ca}}{\omega_b}\frac{dv_{d1}}{dt} = i_{dc1} + \omega_e C_{ca} v_{q1}, \quad \frac{C_{ca}}{\omega_b}\frac{dv_{q1}}{dt} = i_{qc1} - \omega_e C_{ca} v_{d1} \tag{6}$$

where subscript 1 and 2 corresponds to bus 2 and bus 3, respectively.

RL Filter on the grid-side converter

$$\frac{L_{filt}}{\omega_b}\frac{di_{d,filt}}{dt} = v_{d1} - v_{d2} - R_{filt}i_{d,filt} + \omega_e L_{filt} i_{q,filt}$$

$$\frac{L_{filt}}{\omega_b}\frac{di_{q,filt}}{dt} = v_{q1} - v_{q2} - R_{filt}i_{q,filt} - \omega_e L_{filt} i_{d,filt} \tag{7}$$

where subscript *filt* stands for filter (see Fig. 2), and 1 and 2 indicate voltage output from the grid-side converter controller (see Fig. 5) and the voltage of bus 1, respectively. The RL load in the *dq*-domain can be described as

$$\frac{L_{load}}{\omega_b}\frac{di_{dL}}{dt} = v_{d1} - R_{load}i_{dL} + \omega_e L_{load} i_{qL}$$

$$\frac{L_{load}}{\omega_b}\frac{di_{qL}}{dt} = v_{q1} - R_{load}i_{qL} - \omega_e L_{load} i_{dL}$$

$$\frac{C_o}{\omega_b}\frac{dv_{d1}}{dt} = i_{dL} + \omega_e C_o v_{q1}, \quad \frac{C_o}{\omega_b}\frac{dv_{q1}}{dt} = i_{qL} - \omega_e C_o v_{d1} \tag{8}$$

where subscript 1 corresponds to bus 3.

3. Voltage-Source-Converter Controller Design

An important part of the WT is the VSC controller shown in Fig. 2. A more detailed block diagram of the VSC controller depicting the respective input and output variables is shown in Fig. 5. Here, P_g^{set} and Q_g^{set} are the set values for the active and reactive power, respectively, for the WT terminal and are the inputs to the VSC controller. The value of P_g^{set} is determined from the WT energy-harvesting characteristic [17] as shown in Fig. 4, which is represented here as a look-up table $P_g^{set}(\omega_r)$ defined in terms of generator rotor speed ω_r.

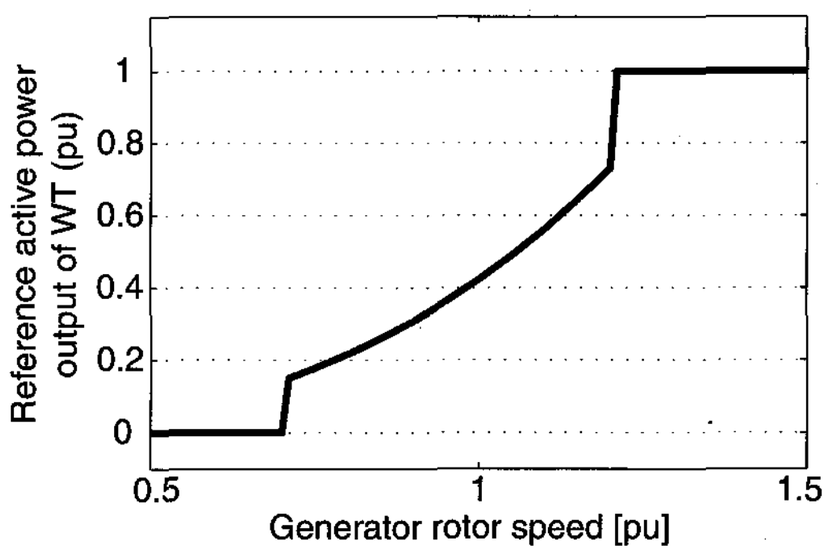

Fig. 4. WT maximum energy-harvesting curve.

When the PFC mode is used, Q_g^{set} is set to zero and all reactive power to the DFIG is provided via the rotor-side converter Q_r. When the LVC mode is used, Q_g^{set} is adjusted by the local controller to maintain the voltage at the WT terminal.

The VSC controller module includes the rotor-side converter controller, the grid-side converter controller, and the dc-link controller as shown in Fig. 5. These controllers utilize conventional proportional-integral (PI) controllers [20]. In this paper, these PI controllers are tuned using the Nyquist constraint technique to deal with model uncertainties [21]. Each of the controllers is briefly described below.

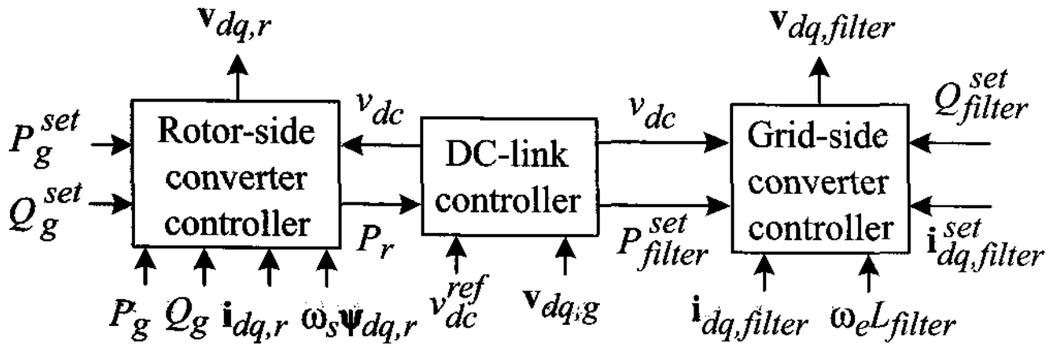

Fig. 5. Block diagram of the VSC controller showing the input/output variables.

3.1 Rotor-Side Converter Controller

Fig. 6 shows a block diagram of the rotor-side converter controller module, which includes four internal PI controllers, PI1 through PI4. The controller is implemented as two branches, one for active power (PI1 and PI2) and one for reactive power (PI3 and PI4) with the corresponding de-coupling terms between the *d* and *q* axes, respectively.

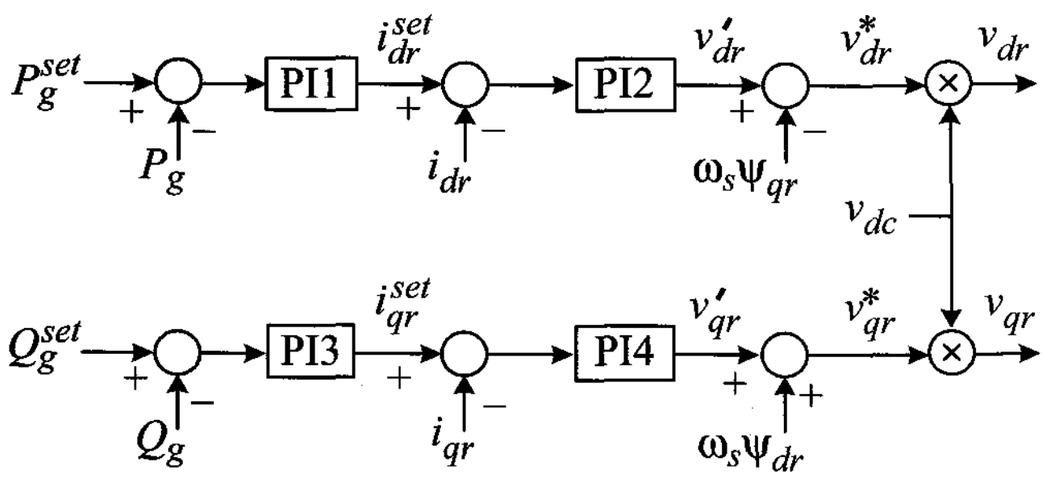

Fig. 6. Block diagram of the rotor-side converter controller.

Using the common assumption of neglecting stator flux transients [20], the transfer function from the rotor voltage to the rotor current is approximated as

$$\begin{bmatrix} \dfrac{I_{dr}(s)}{V'_{dr}(s)} & \dfrac{I_{qr}(s)}{V'_{qr}(s)} \end{bmatrix}^T = \begin{bmatrix} \dfrac{1}{R_r + s(L_r/\omega_b)} & \dfrac{1}{R_r + s(L_r/\omega_b)} \end{bmatrix}^T \tag{9}$$

Similarly, the transfer function from the rotor current to reactive and active power is approximated as

$$\begin{bmatrix} \dfrac{P_g(s)}{I_{dr}(s)} & \dfrac{Q_g(s)}{I_{qr}(s)} \end{bmatrix}^T = \begin{bmatrix} \hat{R}_r + s\hat{L}_r & \hat{R}_r + s\hat{L}_r \end{bmatrix}^T \tag{10}$$

where $\hat{R}_r = \dfrac{(\omega_s - 1)}{\omega_s}\left(\dfrac{R_r}{\omega_b}\right)$ and $\hat{L}_r = \dfrac{(\omega_s - 1)}{\omega_s}\left(\dfrac{L_r}{\omega_b}\right)$, which are obtained from the relation of $P_r \approx -\omega_s P_s$ and $P_g \approx (1-\omega_s)P_s$. Then, (9) is used to tune PI2 and PI4, and (10) is used to tune PI1 and PI3.

3.2 Grid-Side Converter Controller

Fig. 7 shows a block diagram of the grid-side converter controller module, which also includes two internal PI controllers PI5 and PI6, with corresponding de-coupling terms between the *d* and *q* axes.

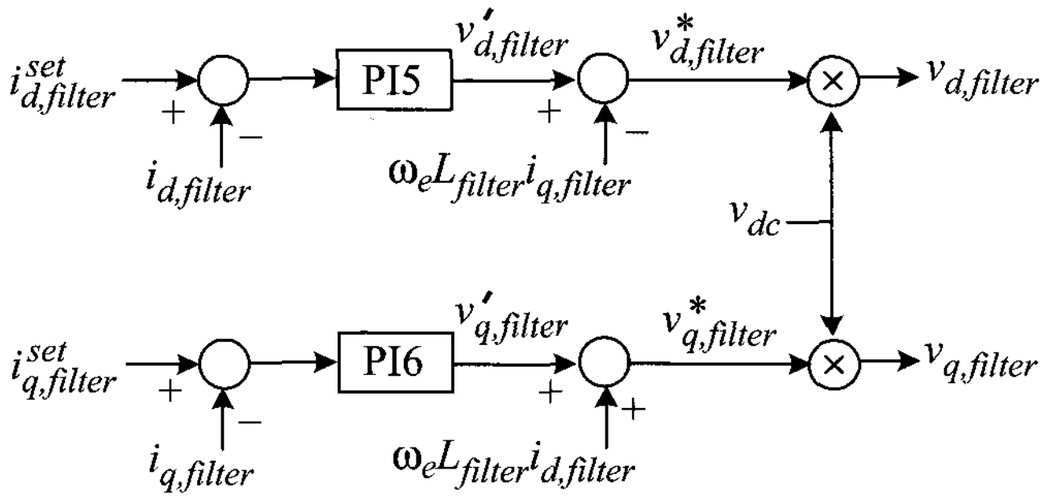

Fig. 7. Block diagram of the grid-side converter controller.

The voltage equation for the grid-side converter RL filter can be expressed as

$$\begin{aligned} \left(\frac{L_{filter}}{\omega_b}\right)\frac{di_{d,filter}}{dt} &= v_{d,filter} - R_{filter} i_{d,filter} + \omega_e L_{filter} i_{d,filter} \\ \left(\frac{L_{filter}}{\omega_b}\right)\frac{di_{q,filter}}{dt} &= v_{q,filter} - R_{filter} i_{q,filter} - \omega_e L_{filter} i_{d,filter} \end{aligned} \tag{11}$$

from which the transfer function from the filter voltage to current is

$$\begin{bmatrix} \dfrac{I_{d,filter}(s)}{V_{d,filter}(s)} & \dfrac{I_{q,filter}(s)}{V_{q,filter}(s)} \end{bmatrix}^T = \begin{bmatrix} \dfrac{1}{R_{filter} + s(L_{filter}/\omega_b)} & \dfrac{1}{R_{filter} + s(L_{filter}/\omega_b)} \end{bmatrix}^T \tag{12}$$

The inputs to the grid-side controller are the set values for the currents, which flows to the gird through the VSC. The set-values of the input currents are calculated by the real and reactive power commands P_{filter}^{set} and Q_{filter}^{set} as follows:

$$\begin{bmatrix} i_{q,filter}^{set} \\ i_{d,filter}^{set} \end{bmatrix} = \begin{bmatrix} v_{q,tr} & v_{d,tr} \\ -v_{d,tr} & v_{q,tr} \end{bmatrix}^{-1} \begin{bmatrix} P_{filter}^{set} \\ Q_{filter}^{set} \end{bmatrix}, \tag{13}$$

where $\mathbf{v}_{qd,tr} = \begin{bmatrix} v_{q,tr} & v_{d,tr} \end{bmatrix}^T$ is the voltage at the low-voltage-side WT transformer; P_{filter}^{set} and Q_{filter}^{set} are the set-point of the real and reactive power commands. The

value for Q_{filter}^{set} is set to zero if the unity power factor control is used; however, P_{filter}^{set} is provided by the dc-link controller, which determines the flow of real power and regulates the dc-link voltage by driving it to a constant reference value.

3.3 DC-link Dynamic Model and Its Controller

The capacitor in the dc-link is an energy storage device. Neglecting losses, the time derivative of the energy in this capacitor depends on the difference of the power delivered to the grid filter, P_{filter}, and the power provided by the rotor circuit of the DFIG, P_r, which can be expressed as

$$\frac{1}{2}\frac{C_{dc}}{\omega_b}\frac{dv_{dc}^2}{dt} = P_r - P_{filter} \tag{14}$$

The dc-link controller regulates the capacitor voltage by driving it to the reference value v_{dc}^{ref}, and outputs the set point for the real power P_{filter}^{set} needed in (13). Fig. 8 shows the dc-link model with its controller PI7. The set point for the output real power by $P_{filter}^{set} = v_{dc} i_{dc,filter}^{set}$.

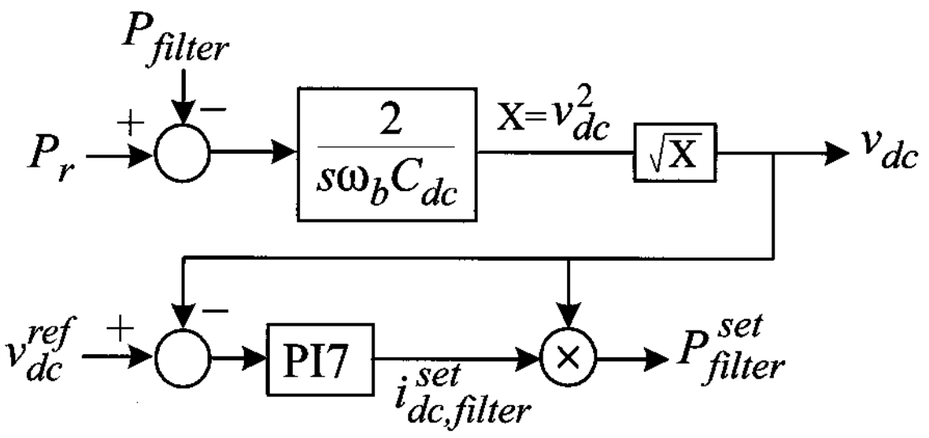

Fig. 8. DC-link model and its controller.

4. Reactive Power Control Design

When controlling WT, it is important that the operating limit of WT is not exceeded. The reactive power required from an individual converter of back-to-back VSC can be computed as

$$Q_j^{set} = \min\left\{Q_j^{\max},\ \Delta Q_{pcc}\right\}, \tag{15}$$

where $j = 1,2$ (here, 1 and 2 stands for rotor-side and grid-side, respectively), $Q_j^{\max}$ is the maximum reactive power (limit) that the j controller can provide, and ΔQ_{pcc} is the total reactive power required to support the voltage at the PCC.

Fig. 9 shows the active- and the reactive-power operating limits, wherein it is assumed that a converter (rotor-side or the grid-side) should not exceed its apparent power limit depicted by the half-circle. Suppose that at a given time the converter is delivering active power denoted herein by P_c, which is changing depending on the wind condition. Then, in addition to the active power, the converter can supply or absorb a maximum of $Q_c^{\max}$ of reactive power. So, the reactive power available from a single converter lies within the limits $\left[-Q_c^{\max};\ +Q_c^{\max}\right]$, which are operating-condition dependent.

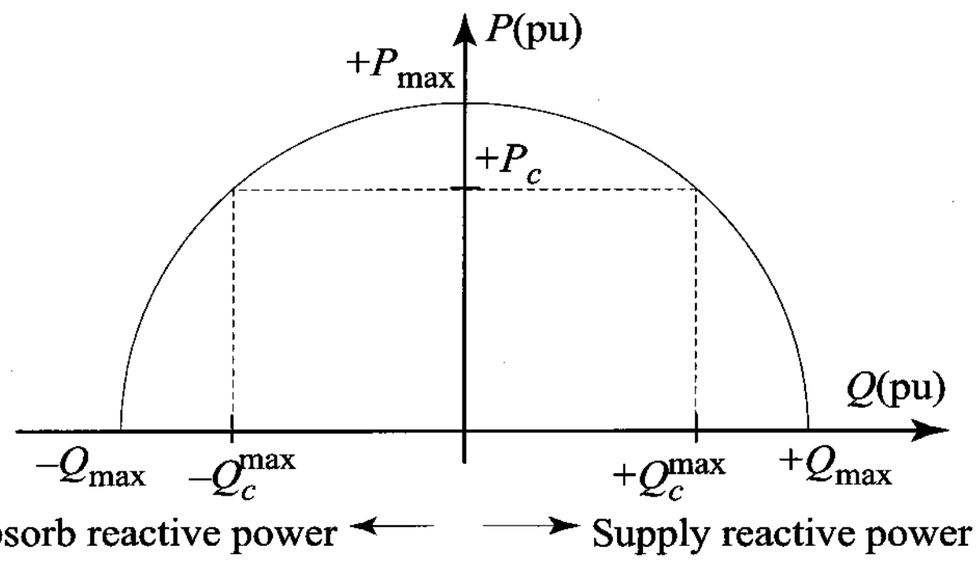

Fig. 9. VSC active and reactive power operating limits.

Since the active power P_c must pass through both the rotor-side and the grid-side converter, and each of them has the limits depicted in Fig. 9. Thus, the maximum available reactive power from the each converter can be expressed as

$$Q_j^{\max} = \sqrt{\left(S_c^{\max}\right)^2 - P_c^2} \tag{16}$$

where it is assumed that the nominal apparent power of the converter is $S_c^{\max}$, defined here as 1/3 of the WT rating [6]. Based on Fig. 9, it also follows that $-S_c^{\max} \le P_c \le S_c^{\max}$. Thus, the reactive power set-point of Q_g^{set} (see Fig. 6) and Q_{filter}^{set} (see Eq. (13)) can be obtained as equated in (16).

To enable a systematic selection of controller gains, it is necessary to find a plant model that represents the relationship between the input and the output with regard to the control objective. Thus, a transfer function from the reactive power injected by the rotor-side converter and the grid-side converter to the change in voltage observed at the PCC is needed.

Although differential and algebraic equations (DAEs) describing all components of the system of Fig. 1 are known and available, straightforward analytical derivation of the required transfer function is not practical due to the

very large size and complexity of the overall system. Instead, the transfer function was extracted from the overall model using numerical linearization available in Simulink [22].

A proportional-plus-integral (PI) controller is considered here since this type of controller is most commonly used in the industry. To ensure that the proposed reactive power control based on PI controller can robustly operate under the changing conditions, a design technique based on the Nyquist constraint is used here to tune the controller gains. Since the detail of control design is beyond scope of this paper, the overall scheme of PI control is only depicted. Since limiting control action should be implemented together with the integrator-anti-windup scheme that would stop integrating the error when the limit is being reached, a PI controller with the proposed distributed anti-windup is implemented in Simulink [22] as shown in Fig. 10 for case studies.

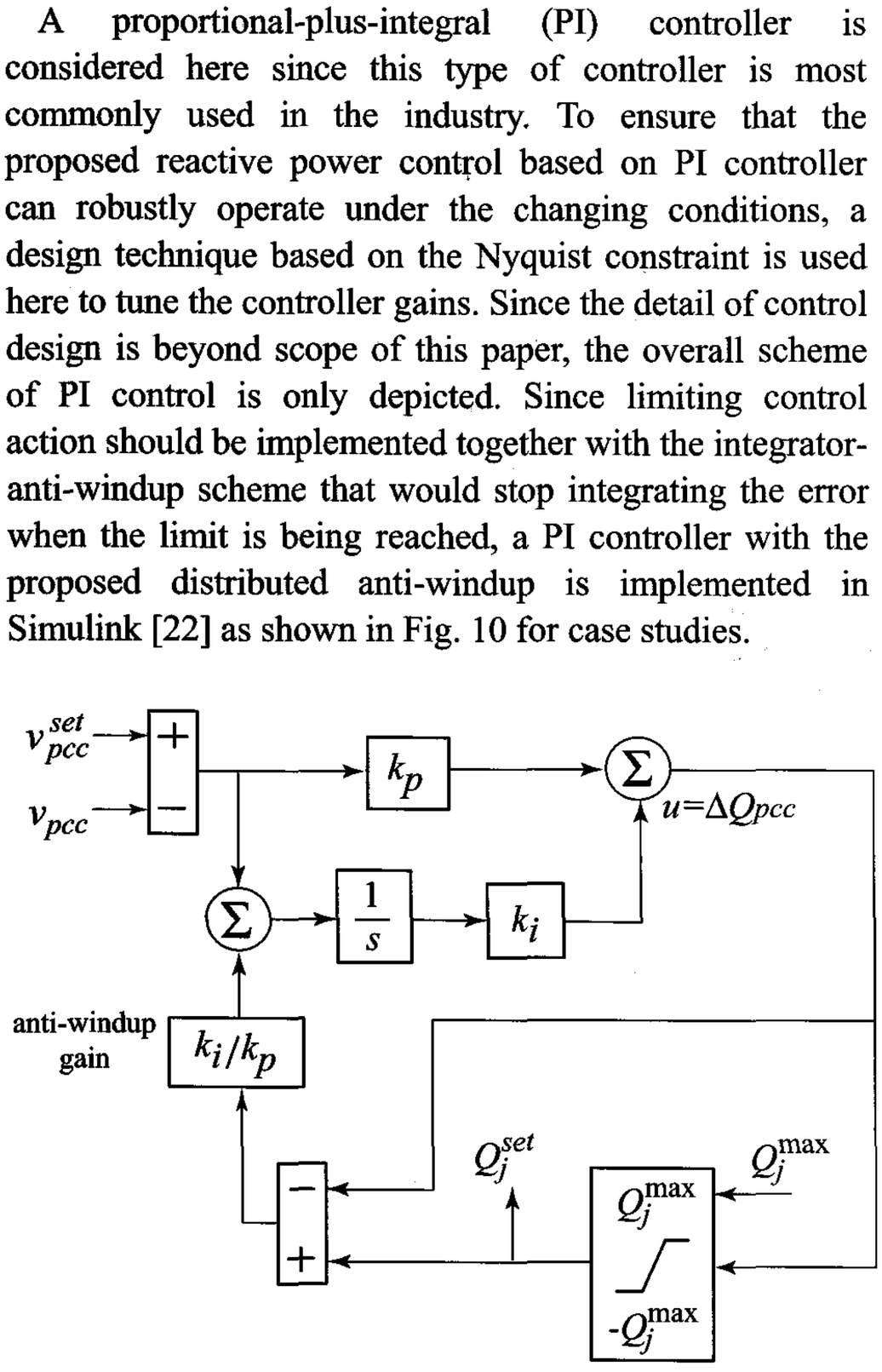

Fig. 10. Implementation of PI controller with the distributed anti-windup.

5. Case Studies

The system in Fig. 1 was implemented in detail using the Matlab/Simulink. Computer studies considering the wind speed variations, the local load variations, and large signal disturbances such as the three-phase symmetrical fault and voltage sag were conducted to compare the dynamic responses of the system with different controls. In comparison, Mode 1 indicates the conventional PFC-mode operation of WT, which Q_g^{set} and Q_{filter}^{set} are set to zero. As another conventional operation, Mode 2 implies that the conventional local voltage control at the terminal of WT where Q_g^{set} is actively utilized while Q_{filter}^{set} is set to zero. Mode 3 is the proposed scheme when both converters are used for voltage control at the PCC; thus, both Q_g^{set} and Q_{filter}^{set} can be instantly utilized.

5.1 Wind-Speed Variation

In this study, the wind speeds shown in Fig. 11 was considered for the WT. Fig. 12 shows the voltage at the PCC, predicted by the model with different controls, respectively. As seen in Fig. 12, the wind speed variations did not represent a problem.

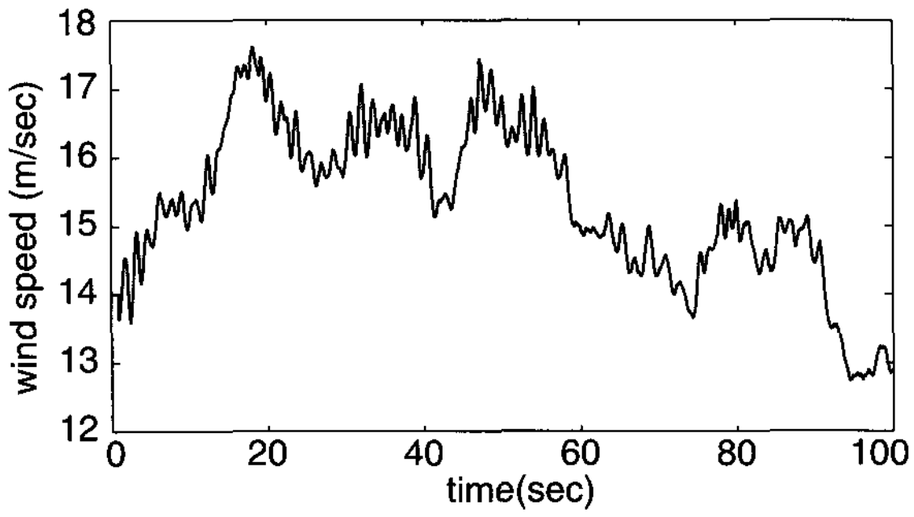

Fig. 11. Wind speed (m/sec).

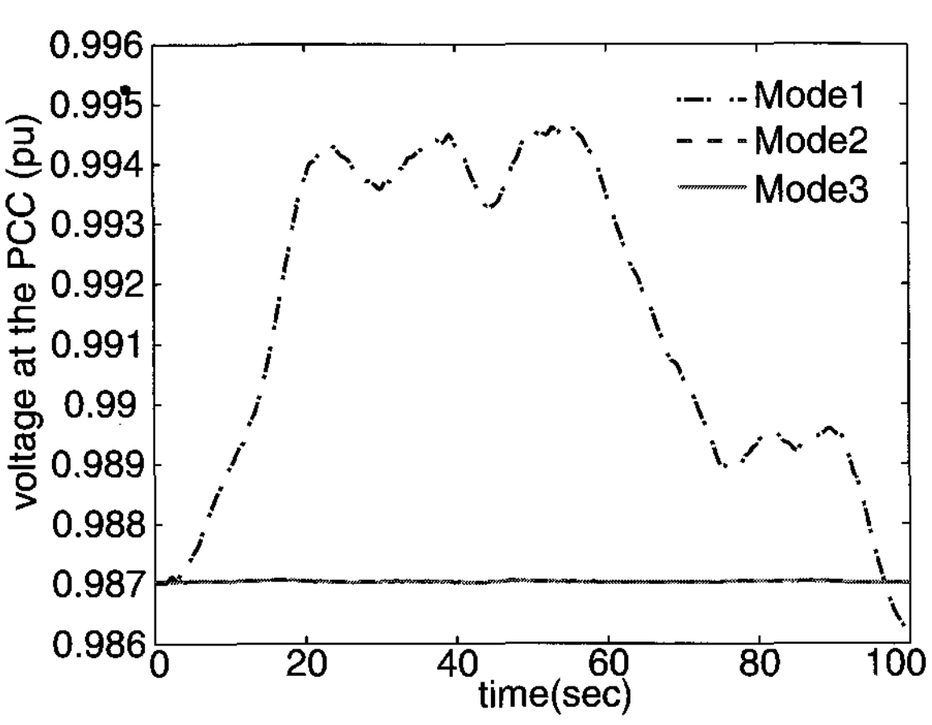

Fig. 12. Voltage observed at the PCC due to the wind speed variation.

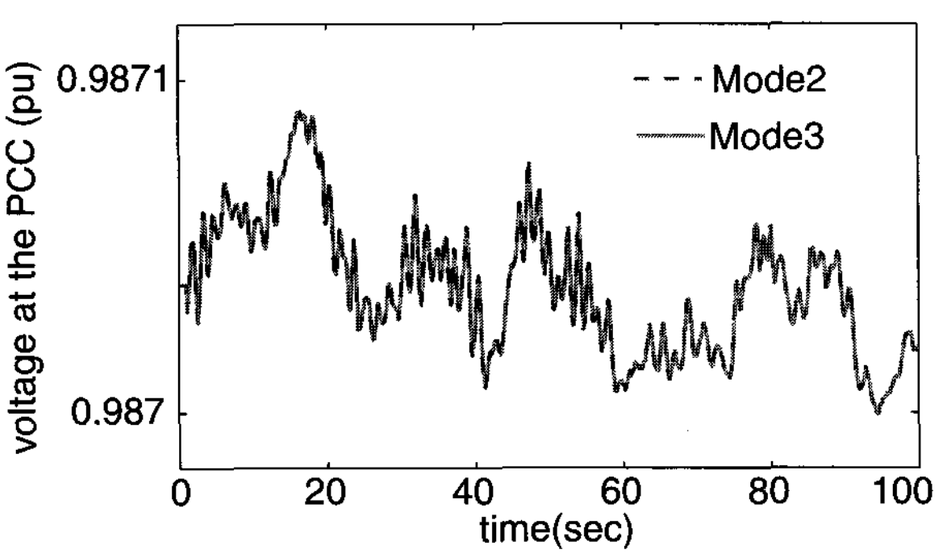

Fig. 12a. Zoomed-in-voltage of Fig.12 in the operation of Mode 2 and Mode 3.

5.2 Local-Load Variation

Two cases were conducted: the local-load impedance by 40% decrease and by 50% decrease. For the case when the local-load impedance is decreased by 40%, the comparison of the voltage transients observed at the PCC was showed in Fig. 13. In the case of 50% decrease of the local-load impedance, the voltage response at the PCC was depicted in Fig. 14. As can be noticed, in Mode 2 and 3 operations, the performance has been significantly improved at the PCC from Mode 1 operation. Also, the voltage has been recovered to its predefined value. In the case of 50% decrease of the local-load impedance, when in the Mode 1, the load impedance changes resulted in noticeable drop of the bus voltage (by 8%). When the WT operated in Mode 2 and 3, the voltage drop was significantly reduced (to 2%). However, the proposed control scheme, Mode 3, performed faster in the bus-voltage recovery at the PCC. Since the maximally available instantaneous reactive-power from both converters was fully utilized, the steady-state errors from Mode 2 and Mode 3 were noticed.

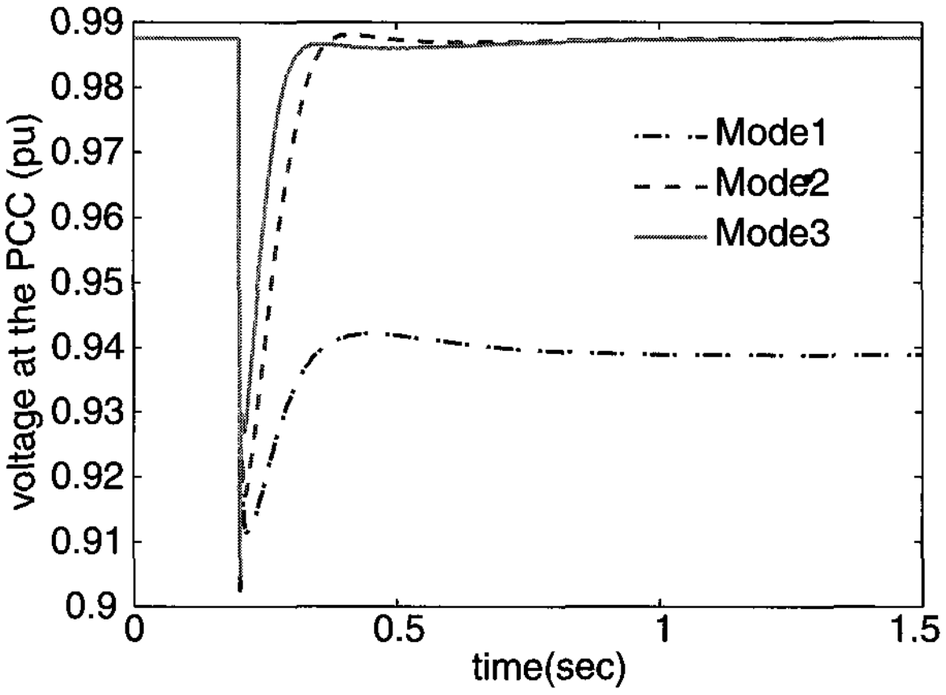

Fig. 13. Voltage observed at the PCC due to the 40% impedance decrease.

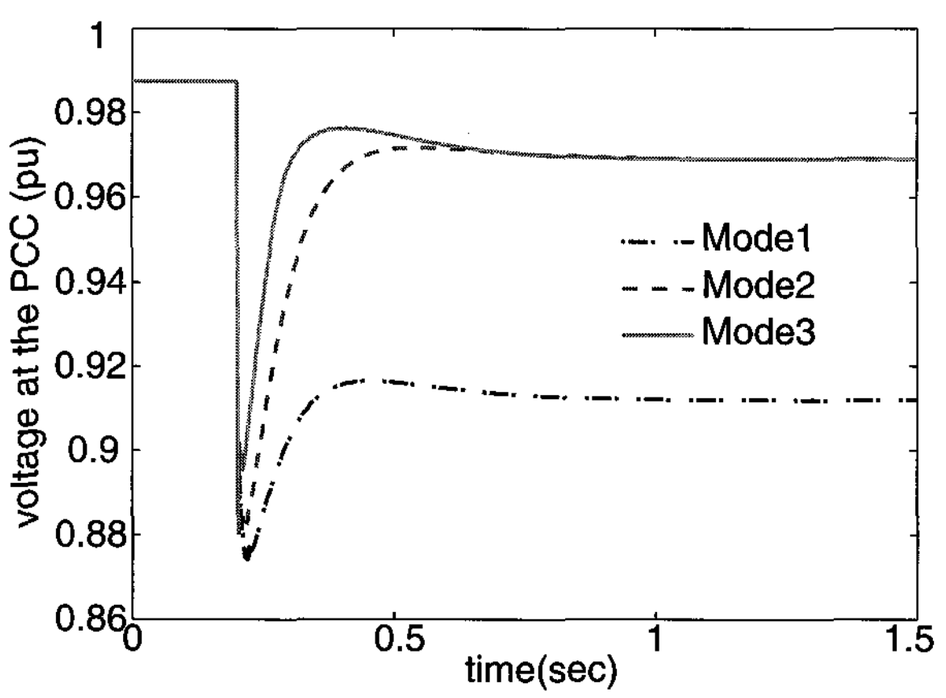

Fig. 14. Voltage observed at the PCC due to the 50% impedance decrease.

5.3 Fault Ride-Through Study

To implement large-signal disturbances, first, a three-phase symmetrical fault was assumed in the middle of TL. To emulate this fault scenario, the fault was assumed at $t = 0.2s$ and was subsequently cleared at $t = 0.7s$ by restoring the initial TL impedance. As can be noted in Fig. 15, the fault resulted in significant voltage swings that can undesirably interfere with the protection circuitry and possibly trip the WT. From this point of view, it is desirable to minimize and/or suppress the voltage swings. During the fault, the voltage drop has been slightly improved in Mode 2 and 3. After the fault was cleared, faster voltage recovery to reach to its predefined voltage at the PCC was noticed in Mode 3.

To consider another large-signal disturbance, voltage sag was assumed at the infinite-bus whose voltage was assumed by 20% decrease from its initial value. As shown in Fig. 16, the voltage deviation by 20% has been noticed in Mode 1 while Mode 2 and 3 resulted in the voltage deviation by 12%. However, Mode 3 showed faster voltage recovery than others.

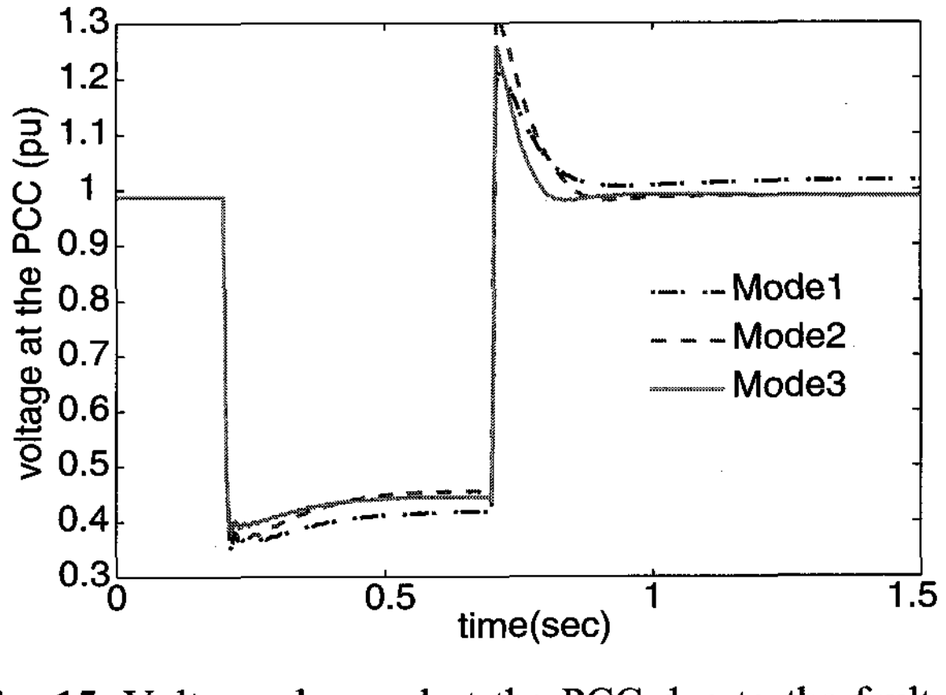

Fig. 15. Voltage observed at the PCC due to the fault at the bus 3.

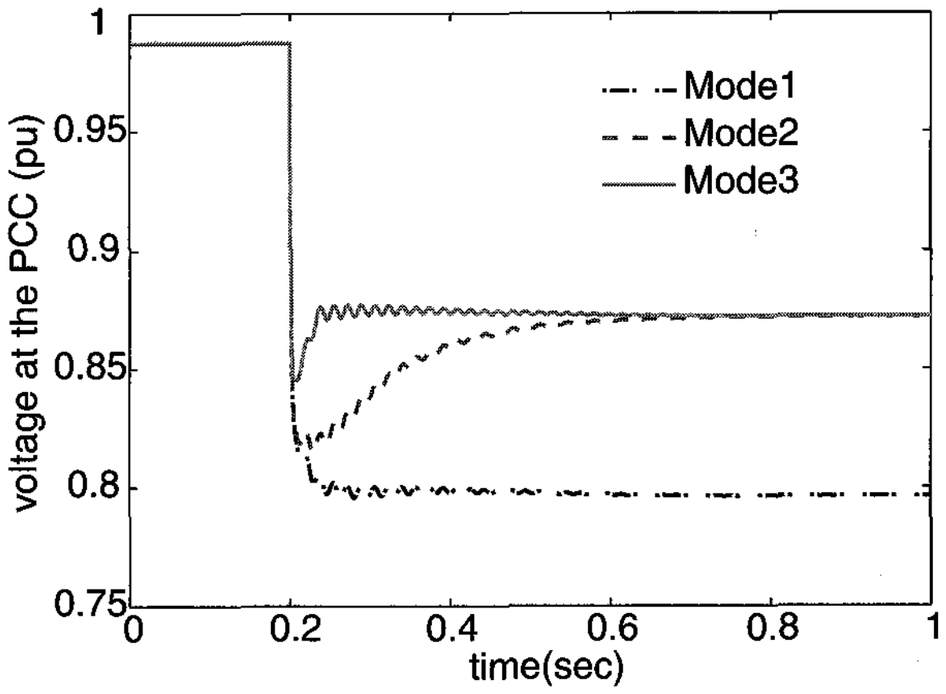

Fig. 16. Voltage observed at the PCC due to the voltage drop at infinite-bus.

5. Conclusion

This paper presented the modeling of DFIG-based variable-speed wind-turbine and demonstrated an advanced voltage control scheme. The goal of investigation was to make use of available wind turbine technology, namely the variable speed doubly-fed induction generator with power electronic converters, to take an active part in improving the voltage control in the system without using additional compensating devices. To ensure reliable operation of the proposed control scheme, the operating-point-dependent reactive power limit of each wind turbine was taken into account.

References

[1] R. Doherty, E. Denny, and M. O'Malley, "System operation with a significant wind power penetration," in *Proc. IEEE Power Engineering Summer Meeting*, vol. 1, 2004, pp. 1002 – 1007.

[2] K. S. Salman and A. L. J. Teo, "Windmill modeling consideration and factors influencing the stability of a grid-connected wind power-based embedded generator," *IEEE Trans. on Power Systems*, vol. 18, no. 2, pp. 793 – 802, May 2003.

[3] Z. Litipu and K. Nagasaka, "Improve the reliability and environment of power system based on optimal allocation of WPG," in *Proc. IEEE Power Systems Conf. and Exposition*, vol. 1, 2004, pp. 524 – 532.

[4] N. Dizdarevic, M. Majstrovic, and S. Zutobradic, "Power quality in a distribution network after wind power plant connection," in *Proc. IEEE Power Systems Conf. and Exposition*, vol. 2, 2004, pp. 913 – 918.

[5] E. ON Netz, *Wind Power Report*, Sept. 2004, Germany.

[6] Elsam Engineering, *BC Wind Integration System Expansion Study*, July 2004.

[7] T. Gjengedal, "Large scale wind power farms as power plants," in *Proc. Nordic Wind Power Conf.*, 2004.

[8] Z. Saad-Saoud, M. L. Lisboa, J. B. Ekanayake, N. Jenkins, and G. Strbac, "Application of STATCOMs to wind farms," in *Proc. IEE Proceedings-Generation, Transmission, and Distribution*, vol. 145, 1998, pp. 511 – 516.

[9] A. Papantoniou and A. Coonick, "Simulation of FACTS for wind farm applications," in *Proc. IEE Colloquium on Power Electronics for Renewable Energy*, 1997, pp. 1 – 5.

[10] L. T. Ha and T. K. Saha, "Investigation of power loss and voltage stability limits for large wind farm connections to a subtransmission network," in *Proc. IEEE Power Engineering Summer Meeting*, vol. 2, 2004, pp. 2251 – 2256.

[11] M. P. Palsson, T. Toftevaag, K. Uhlen, and J. O. G. Tande, "Large-scale wind power integration and voltage stability limits in regional networks," in *Proc. IEEE Power Engineering Summer Meeting*, vol. 2, 2002, pp. 762 – 769.

[12] ENERCON GmbH, *Wind Turbine* E-112. Available: http://www.enercon.de/en/_home.htm (Jan. 8, 2006).

[13] T. Senjyu, N. Sueyoshi, R. Kuninaka, K. Uezato, H. Fujita, and T. Funabashi, "Study on terminal voltage and power factor control of induction generator for wind power generation system," in *Proc. International Conf. on Power System Technology*, vol. 1, 2004, pp. 753 – 758.

[14] T. Sun, Z. Chen, and F. Blaabjerg, "Transient analysis of grid-connected wind turbines with DFIG after an external short-circuit fault," in *Proc. Nordic Wind Power Conf.*, 2004.

[15] T. Senjyu, T. Kinjo, H. Fujita, and Aichi, "Analysis of terminal voltage and output power control of wind turbine generator by series and parallel compensation using SMES," in *Proc. IEEE 35th Annual Power Electronics Specialists Conf.*, vol. 6, 2004, pp. 4278 – 4284.

[16] Y. Kubota, T. Genji, K. Miyazato, N. Hayashi, H. Tokuda, and Y. Fukuyama, "Verification of cooperative control methods for voltage control equipment on distribution network simulator considering interconnection of wind power generators," in *Proc. IEEE Transmission and Distribution Conf. and Exhibition*, vol. 2, 2002, pp. 1151 – 1156.

[17] T. Ackermann, *Wind Power in Power Systems*, John Wiley & Sons, Ltd., UK, 2005.

[18] H. S. Ko, "Supervisory voltage control scheme for grid-connected wind farms," Ph.D. dissertation, Dept. Elect. and Comp. Eng., Univ. of British Columbia, Vancouver, BC, Canada, 2006.

[19] P. C. Krause, O. Wasynczuk, and S. D. Sudhoff, *Analysis of Electric Machinery and Drive Systems*, John Wiley & Sons Inc., New Jersey, 2002.

[20] R. Pena, J. C. Clare, and G. M. Asher, "Doubly fed induction generator using back-to-back PWM converters and its application to variable-speed wind-Energy Generation," in *Proc. IEEE Electric Power Application Proceeding*, vol. 143, No. 3, 1996, pp. 231 – 241.

[21] K. Åström and T. Hägglung, *PID Controllers,* Lund Institute of Technology, 2004.

[22] Matlab and Simulink, MathWorks, Jan. 2000.

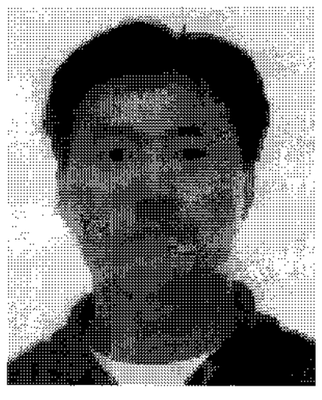

Hee-Sang Ko

He received his B.S. degree in Elect. Eng. from Jeju National Univ., Jeju, Korea, in 1996, his M.Sc. degree in Elect. Eng. from Pennsylvania State Univ., University Park, USA, in 2000, and his Ph.D. in Electrical and Computer Eng. from the Univ. of British Columbia, Vancouver, Canada, in 2006. He was a researcher in the wind energy research center at Korea Institute of Energy Research (KIER), Daejeon, Korea. His research interests include wind power generation, power systems voltage and transient stability, data processing for power systems security analysis, electricity market analysis, control design, and system identification.

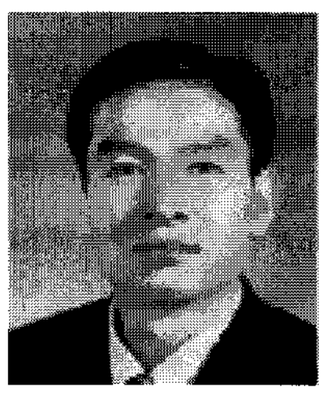

Gi-Gab Yoon

He received his B.S., M.Sc., and Ph.D. degree in Elect. Eng. from Hanyang Univ., Seoul, Korea, in 1983, 1988, and 1999. He is a senior researcher in power system laboratory and advanced distribution system group at KEPRI.

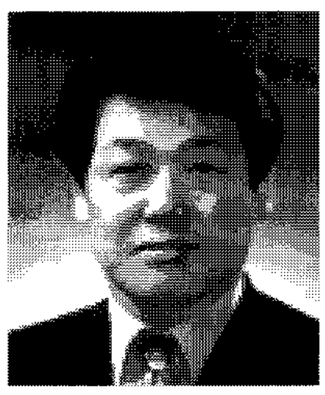

Won-Pyo Hong

He received his B.S degree in Electrical Engineering from Sungsil University, Seoul, Korea, in 1978, his M.Sc. and Ph.D. degree in Elect. Eng. from Seoul National Univ., Seoul, Korea, in 1980 and 1989. From 1980 to 1993 he was employed as senior researcher number at the Power System Lab. of KEPRI. From 1993, he is a professor of the Depart. of Building Services Eng. at the Hanbat National Univ. His research activities are in the areas of the building and industrial application of fieldbus, energy management, building automation and control, intelligent networked control and control & planning of distributed energy resource.